Zhang Zhaoliang (Orcid ID: 0000-0002-8048-0600)

/   /

Electrocatalytic conversion of lithium polysulfides by highly dispersed ultrafine Mo₂C nanoparticles on hollow N-doped carbon flowers for Li-S batteries

Rameez Razaq, Nana Zhang, Ying Xin, Qian Li, Jin Wang, Zhaoliang Zhang*

Dr. R. Razaq, N. Zhang, Dr. Y. Xin , Dr. Q. Li, Dr. J. Wang, Prof. Dr. Z. Zhang

School of Chemistry and Chemical Engineering, Shandong Provincial Key Laboratory of Fluorine Chemistry and Chemical Materials, University of Jinan, Jinan 250022, China.

E-mail: chm_zhangzl@ujn.edu.cn

Dr. R. Razaq

University of Michigan-Shanghai Jiao Tong University Joint Institute, Shanghai Jiao Tong University, 800 Dong Chuan Road, Minhang District, Shanghai 200240, China

Prof. Dr. Z. Zhang

Institute of Catalysis for Energy and Environment, College of Chemistry and Chemical Engineering, Shenyang Normal University, Shenyang 110034, Liaoning, China

Keywords: lithium-sulfur battery, electrocatalysis, ultrafine Mo₂C, 3D nanostructure, polysulfide conversion

The significant challenge in exploring novel nanostructured sulfur host materials for Li-S batteries is to simultaneously mitigate the notorious shuttle effect and catalytically enhance the

redox kinetics of lithium polysulfides (LPSs). Herein, a novel ultrafine Mo_2C nanoparticles uniformly distributed on 2D nanosheet-assembled 3D hollow nitrogen doped carbon flowers (HNCFs) is designed. The Mo_2C/HNCFs architecture with unique flower-like morphologies not only efficiently suppressed the aggregation of 2D nanosheets but also highly distributed the ultrafine Mo_2C nanoparticles that act as catalytic active sites for efficient adsorption and conversion of LPSs. Furthermore, the 3D hierarchical arrangement can afford ample internal space to accommodate sulfur species, large volume expansion, 3D electron pathway, and physical/chemical blockage of LPSs to reduce the loss of active materials. The Mo_2C/HNCFs composite exhibits a high rate capability, unprecedented capacity retention of 92% over 100 cycles at 0.5C placing Mo_2C/HNCFs one of the best LPSs adsorbents and electrocatalysts.

1. Introduction

To address the challenges of current environmental pollution and energy crisis, alternative energy technologies are urgently demanded to substitute traditional fossil fuels, e.g. lithium sulfur batteries (LSBs),[1] which have been touted as the upcoming post lithium ion batteries (LIBs) due to the remarkably high theoretical specific energy density of 2600 W h kg^{-1} and low cost of nontoxic elemental sulfur.[2] On the other hand, tons of thousands of sulfur are produced as a by-product of the petroleum refining process [3] and by the reduction of SO_2 during flue gas purification.[4] Furthermore, the recovered sulfur from H_2S by Clause process need to find a valuable and green usage.[5] Being sulfur cathode for LSBs is right a good choice. However, the practical application of the LSBs are hindered by the shuttle effect and the sluggish redox kinetics of LPSs.[6,7] Recently, a great amount of research has shown that the electrochemical performances in LSBs are heavily dependent on electrocatalytic conversion of LPSs.[6, 8-10] The

electrocatalysts during the discharge process accelerate the transformation from soluble LPSs to insoluble Li_2S_2/Li_2S by lowering the overpotential.[9] As the fast conversion reactions decrease the detention time of soluble LPS (long detention times cause severe losses of active materials) thereby suppressing dissolution.[9] Meanwhile, during the charge process electrocatalysts reduce the potential hill at initial charging originating from the phase nucleation of Li_2S_2/Li_2S and improve the oxidation kinetics and sulfur utilization.[10-12] In this perspective, several pioneer works have been performed on various electrocatalysts, such as Pt/G,[13] Mo_2C/CNT,[14] ZnS_{1-x}/rGO,[15] CP@NCNT@CoS_3,[16] (Co−N/G),[11] h-TiN,[17] porphyrin (POF),[18] Co_3S_4,[10] VO_2 and VS_2 nanosheets,[19] Fe_3C/Fe-N_x,[20] CoP nanoparticles[21] and Fe_2O_3@N-PC/Mn_3O_4.[22] However, the investigation of polysulfide electrocatalysis is still at its early stage, with neither systematic designed electrocatalyst nor deep mechanism understanding. Henceforth, novel and unique nanostructured electrocatalysts are strongly demanded in order to establish electrocatalytic chemistry of sulfur-containing compounds for the practical application of LSBs.

Most importantly the previously reported electrocatalysts for LSBs are either micro-sized or bulk crystals, imposing restriction on available active sites for catalysis or adsorption towards LPSs.[14,23,24] Reducing the dimensions of electrocatalysts is a potential solution to this issue. In this case, nano-sized transition metal carbides (TMCs) on 2D (two dimensional) structure will be attractive due to the large exposed active surface and sites for sulfur coverage and conversion. Particularly, molybdenum-based carbide (Mo_2C) attracts a huge interest considering its strong polarity, promising conductivity and efficient electrocatalytic ability.[25,26] Unfortunately, the high reaction temperature for the preparation of Mo_2C induces extensive particle sintering, leading to big particle dimension and low surface areas that are not suitable for practical

3

applications.[27] In order to mitigate sintering, Mo_2C nanoparticles are usually dispersed on conductive supports such as carbon nanotubes or graphene nanosheets. Nevertheless, these 1D (one-dimensional)[23] or 2D carbon supports[28] themselves are prone to entangle or aggregate, which may risk negating all the advantages associated with the small Mo_2C nanoparticle size. Therefore, the controllable synthesis of small-sized, well dispersed, and electrochemically accessible ultrafine Mo_2C nanoparticles uniformly distributed on 3D (three-dimensional) structured-carbon remains challenging at present.

Herein, we designed a novel 3D nanostructured sulfur host comprising of ultrafine Mo_2C nanoparticles on hollow N-doped carbon flowers (HNCF) for LSBs. The uniformly distributed Mo_2C nanoparticles act as catalytic active site for efficient adsorption and redox conversion of LPSs. Meanwhile, the HNCFs can afford ample internal space to: i) accommodate sulfur species, ii) allow large volume expansion, iii) provide 3D electron pathway, iv) reduce the loss of active materials via physical/chemical blockage and v) the flowerlike architecture can effectively avoid lamellar stacking and particle aggregation[29] Significantly, the strong interaction between the ultrafine Mo_2C and HNCFs enhanced the redox kinetics and charge transfer of the sulfur electrode. Owing to unique structural design, the Mo_2C/HNCFs composite delivers a capability of 1181 and 572 mA h g^{-1} at 0.2 C and 4 C, respectively and extraordinary capacity retention of 92% over 100 cycles at 0.5 C. The present work highlights the importance of designing the novel 3D structure and ultrafine Mo_2C nanoparticles as efficient active sites on HNCFs for enhancing adsorption and redox conversion of LPSs.

2. Results and Discussion

The synthesis of ultrafine Mo_2C nanoparticles on HNCFs are briefly outlined in Scheme 1. Colloidal silica spheres were first prepared using the classic Stöber method (Figure S1).[30] Typically, the SiO_2, $Mo_7O_{24}^{6-}$ anions and dopamine (DA) were successively mixed in water and ethanol mixture. Afterward, the appropriate volume of aqueous ammonia was added to trigger the spontaneous polymerization of DA together with $Mo_7O_{24}^{6-}$ (Mo/PDA). The interaction between Mo/PDA and SiO_2 was facilitated by the catechol and amine functional groups, resulting in coating of Mo/PDA onto the surface of SiO_2. Interestingly, Mo completely changed the growth behavior of PDA into 2D layers, and eventually leading to the formation of Mo/PDA with unique microflower morphology. Finally, SiO_2@Mo/PDA was calcined at 800 °C in Ar and SiO_2@Mo_2C/HNCFs was obtained, which was then etched by NaOH solution to remove SiO_2. The sulfur was loaded into the as-prepared Mo_2C/HNCFs by vapour phase infusion method.

Figure 1a shows the typical X-ray diffraction (XRD) pattern of Mo_2C/HNCFs. In addition to a characteristic diffraction peak (002) of carbon at $2\theta = 24°$, several sharp peaks corresponding to Mo_2C (JCPDS 77-0720) were confirmed. The morphology of the as-synthesized nanostructure Mo_2C/HNCFs was firstly examined by Field emission scanning electron microscopy (FESEM) equipped with Energy dispersive spectroscopy (EDS) showing hollow carbon flowers with average diameter of ~1.6 μm (Figure 1b). Furthermore, each micro-flower was formed from the assembly of hundreds of thin 2D nanoflakes vertically aligned with sufficient space between neighboring nanoflakes (Figure 1c). The content of Mo_2C in the Mo_2C/NHCFs hybrid obtained by EDS is estimated to be ~53 wt.% (Figure S2). The unique 3D structure of Mo_2C/HNCFs with numerous nanoflakes and nanovoids is also confirmed by

5

Transmission electron microscopy (TEM) (Figure 1d). Furthermore, a large number of ultrafine particles are uniformly dispersed over the carbonaceous nanoflakes (Figure 1e). The high-resolution TEM (HRTEM) image shows that these ultrafine particles possess an average size of ~1.6 nm with an interlayer spacing of 0.23 nm, corresponding to (101) plane of Mo_2C (Figure 1e, inset), consistent with the XRD result. For a control sample, the XRD pattern of HNCS shows two diffraction peaks at 2θ of 24 and 44°, which could be indexed to the (002) and (101) diffraction planes of carbon (Figure S3a), suggesting the mostly amorphous nature of the HNCS. The morphology of the HNCSs is characterized by FESEM which demonstrates the hollow spheres (Figure S3b).

The obtained Mo_2C/HNCFs was further analysed by X-ray photoelectron spectroscopy (XPS). The XPS survey of Mo_2C/HNCFs displays well-resolved peaks of C, N, Mo, and O species (Figure 2a). Specifically, the deconvoluted C 1s spectrum (Figure 2b) can be attributed to sp^2-hybridized C-C/C=C, C-N and C=O species.[31] From the N1s spectrum, three N species referring to the pyridinic, pyrrolic and graphitic were observed (Figure 2c), manifesting the multiconfiguration of N heteroatom doping in the carbon lattice.[27,32] The Mo 3d XPS spectrum is derived from Mo_2C ($3d_{5/2}$ at 228.2 eV), MoO_2 ($3d_{5/2}$ at 229.0 eV) and MoO_3 ($3d_{5/2}$ at 232.4 eV) (Figure 2d). The presence of a significant quantity of oxides seems to be unavoidable for carbide materials due to their oxidation at the surface upon exposure to air.[33] However, according to previous results, the oxide passivation layer on Mo_2C may contribute to adsorb polysulfides.[34]

To investigate the electrochemical properties of Mo_2C/HNCFs, sulfur was loaded into the Mo_2C/HNCFs by a vapour phase infusion method (S-Mo_2C/HNCFs). SEM images show that

6

the S-Mo_2C/HNCFs composite well maintains the original morphology after sulfur loading (Figure 3a, b and Figure S4), demonstrating the homogeneous loading of sulfur into the Mo_2C/HNCFs structure. Furthermore, EDS elemental mapping (Figure 3c-g) and XRD (Figure 3h) (S_8, JCPDS 08-0247) of S-Mo_2C/NHCFs reveal that sulfur is evenly distributed in the Mo_2C/HNCFs host. The sulfur loading in S-Mo_2C/HNCFs composite was determined by Thermo-gravimetry analysis (TGA), that is 69 wt.% (Figure 3i, Figure S5). In comparison, the sulfur loaded onto the HNCSs as a control sample (by vapour phase infusion method), denoted as S-HNCSs, was confirmed by FESEM (Figure S6) and XRD (Figure S7) with 63 wt.% sulfur loading as determined by TGA (Figure S8).

To evaluate the advantages of the Mo_2C/HNCFs as an advanced sulfur host for LSBs, 2025-type coin cells using S-Mo_2C/HNCFs and S-HNCSs as cathodes and lithium metal as anodes were assembled. Figure 4a shows the cyclic performance of S-Mo_2C/HNCFs and S-HNCS. The S-Mo_2C/HNCFs electrode retained a discharge capacity of 902 mAh g^{-1} after 100 cycles with 92.7% capacity retention and 0.07% capacity decay per cycle merely. The Coulombic efficiency is $\sim$100%. In contrast, S-HNCS retained a discharge capacity of 494 mAh g^{-1} with low capacity retention after 100 cycles. From Nyquist plots (Figure 4b), it can be observed that the S-Mo_2C/HNCFs electrode has a smaller semicircle in the high-frequency region, indicating the lower charge transfer resistance compared with S-HNCSs. Long cycling performance was investigated to demonstrate the superior lifetime of S-Mo_2C/HNCFs at high current rate (1 C). After 300 cycles, the S-Mo_2C/HNCFs cathode exhibits specific capacity of 585 mAh g^{-1} with a capacity decay of 0.08% per cycle and $\sim$100% Coulombic efficiency (Figure 4c). However, S-HNCS retains a capacity of only 257 mAh g^{-1} with 0.11% capacity decay per cycle (Figure S9).

7

Figure 4d shows the rate performance of the S-Mo$_2$C/HNCFs cathode, where the specific capacities at the current densities of 0.2 C, 0.5 C, 1 C, 2 C, and 4 C were 1181, 1037, 879, 738, and 572 mA h g^{-1}, respectively. The excellent capacity reversibility to 928 mA h g^{-1} was achieved at 0.5 C. In contrast, S-HNCS shows low rate performance at the same current densities (Figure S10). Figure 4e shows the galvanostatic charge-discharge profiles of the S-Mo$_2$C/HNCFs electrode at different current rates (0.2 C to 4 C). Two reaction plateaus can be evidently observed in the discharge process that correspond to the reduction of sulfur into long-chain LPSs and the subsequent formation of short-chain LiPSs to Li$_2$S, respectively, whereas the charge plateau is attributed to the transformation of Li$_2$S$_2$/Li$_2$S to Li$_2$S$_8$/S$_8$. Prominently, the galvanostatic charge/discharge voltage profile of S-Mo$_2$C/HNCFs at 4 C is still obvious. However, S-HNCS cannot maintain the charge plateau even at 1 C (Figure S11). Since high mass loading of active materials are essential for the energy density of LSBs, a thicker S-Mo$_2$C/HNCFs electrode with areal sulfur loading of 3.1 mg cm^{-2} is further evaluated (Figure 4f). Upon cycling at 0.5 C, a high discharge capacity of 613 mAh g^{-1} is delivered, corresponding to ∼100% capacity retention and Coulombic efficiency. The capacity rise during the initial cycles is attributed to gradually wetting of the thicker 3D porous cathode by electrolyte which smooths the ion diffusion.[35] Comparatively, S-HNCS exhabits a discharge capacity of 282 mAh g^{-1} only (Figure S12).

The excellent electrochemical properties of Mo$_2$C/HNCFs is anticipated to be derived from strong adsorption and efficient catalytic conversions of LPSs.[9,18] In this perspective, static adsorption tests of Mo$_2$C/HNCFs and HNCSs for LPSs were first performed. When Mo$_2$C/HNCFs was added into a Li$_2$S$_4$ solution, a change in color was observed (Figure 5a);

8

however, HNCSs could not decolorize Li_2S_4 solution, indicating that Mo_2C/HNCFs exhibited strong adsorption capability for Li_2S_4 molecules.[36,37]

Secondly, the electrochemical polarization was performed in order to confirm the redox kinetics of S-Mo_2C/HNCFs and S-HNCSs electrodes. Figure 5b shows the flatter and longer discharge plateaus for S-Mo_2C/HNCFs with a higher discharge/charge capacity and a smaller hysteresis (ΔE = 134 mV) in comparison with S-HNCS (ΔE = 310 mV), suggesting the enhanced electrochemical performance and accelerated redox kinetics in S-Mo_2C/HNCFs. In addition, the improved electrochemical kinetics was observed in the discharge (Figure 5c) and charge (Figure 5d) processes during phase change between the soluble LPSs and insoluble Li_2S_2/Li_2S. Figure 5c displays the discharge plateau, which confirms the overpotential for the conversion of soluble Li_2S_4 to insoluble Li_2S_2/Li_2S.[9,38] The S-HNCSs electrode shows a large overpotential of 55 mV, suggesting that a high interfacial energy barrier existed for Li_2S nucleation and deposition on the surface.[11,16] In contrast, the Li_2S nucleation behavior is quite different in the case of S-Mo_2C/HNCFs (Figure 5c). The S-Mo_2C/HNCFs electrode exhibits a significantly reduced interfacial energy barrier of 18 mV, indicating the facilitation of Li_2S nucleation and deposition process (Figure 5c). Likewise, Figure 5d shows the charge plateaus, from which the overpotential and potential barrier for the conversion of insoluble Li_2S to soluble LPSs can be assessed.[11,12] The S-HNCSs cathode exhibits a high overpotential and potential barrier at about 2.39 V in the charging process, indicating a sluggish activation process.[12,19] However, the combination of uniformly distribution of ultrafine Mo_2C nanoparticles with HNCFs significantly reduces the height of the potential barrier to 2.31V (Figure 5d).[11,19] This strong synergism is favorable for lowering the overpotential and

improving capacity compared with HNCSs only. These findings provide insight into a fundamental understanding of ultrafine Mo_2C nanoparticles on HNCFs for catalytical conversion of LPSs.

Thirdly, the symmetric cells were configured using Mo_2C/HNCFs or HNCSs as identical working and counter electrodes, within a voltage range of -0.7 to +0.7 V (vs Li/Li^+) to check its catalytic ability.[39] The fabrication of symmetric cells eliminates the lithium metal anode and hence provide direct analysis of the polysulfides redox conversion in the hierarchical electrode. As observed in Figure 5e, the Mo_2C/HNCFs symmetric cell exhibits the higher polarization current compared with HNCSs, indicating that Mo_2C/HNCFs provides the better catalytic performance, which is the direct evidence of polysulfide electrocatalytic conversion on Mo_2C/HNCFs.[40] Furthermore, the EIS measured on symmetric cells revealed a lower resistance for Mo_2C/HNCFs in comparison with HNCFs, which is another indication of the electrocatalytic effects derived from the unique flower-like 3D Mo_2C/HNCFs with unique uniformly dispersed ultrafine Mo_2C nanoparticles (Figure 5f). The robust catalytic effect of Mo_2C/HNCFs is due to highly distributed ultrafine Mo_2C nanoparticles that provide more catalytic active sites for efficient adsorption and conversion of LPSs.[41,42]

Fourthly, Cyclic voltammetry (CV) curves for S-Mo_2C/HNCFs and S-HNCS were performed at different scan rates ranging from 0.1 to 0.4 mV s^{-1} (Figure S13, S14), which exhibit two cathodic peaks (I and II) and one anodic peak (III). The higher current density for S-Mo_2C/HNCFs at different scan rates (Figure 6a and b) suggests the bigger decrease of polarization due to the participation of active Mo_2C in the redox reactions in comparison with S-HNCS (Figure 6c, d), consistent with discharge/charge profiles. Furthermore, with an

10

increase in the scan rate, the S-Mo₂C/HNCFs electrode shows a less decrease in onset potentials

for peaks I and II, and III than that for S-HNCS, implying that the sulfur redox reaction on the

surface of Mo₂C/HNCFs was accelerated (0.05 *vs* 0.06, 0.09 *vs* 0.14, 0.09 *vs* 0.14).[17,43] The

superb catalytic activity revealed by the Mo₂C/HNCFs with regards to LPSs conversion could

be further demosnstrates by its lower Tafel slope that is 80 mV dec⁻¹ compared with 134 mV

dec⁻¹ for HNCS, obtained by anaylzing the CV curve at 0.1 mV s⁻¹ (Figure 6e, f).[44] Additionally,

as shown in Figure 6g-i, all cathodic and anodic peak currents are linear with the square root of

scan rates, from which the lithium diffusion performance can be estimated using the classical

Randles Sevcik equation:[45]

$$I_p = (2.69 \times 10\,5)\, n^{1.5}\, S\, D_{Li^+}\, 0.5\, C_{Li}\, v^{0.5}$$

where I_P is the peak current, n is the charge transfer number, S is the surface area of the

electrode, D_{Li^+} is the lithium ion diffusion coefficient, C_{Li} is the concentration of lithium ions,

and v is the scan rate. Because n, S, and C_{Li} are unchanged, the slope of the curve ($I_p/v^{0.5}$)

represents the Li⁺ ions diffusion rate. At any conditions, the slopes of curves for S-

Mo₂C/HNCFs are higher than those for S-HNCSs (Figure 6g-i), suggesting that S-

Mo₂C/HNCFs show better diffusion properties compared with S-HNCSs. The enhanced Li⁺

ions diffusion promotes the catalytic effect of Mo₂C/HNCFs, which is critical in improving the

battery performance.

The catalytic effects of the ultrafine Mo₂C nanoparticles on HNCF is schematically

illustrated in Figure 7a, where the strong adsorption for LPSs is the first step of catalytic

conversions. To validate the morphology integrity of Mo₂C/HNCFs after long cycling, the

electrode film from disassembled cells at fully charged status is re-examined by SEM and

HRTEM. As shown in Fig. 7b and c, the individual $Mo_2C/HNCFs$ flower is retained and the component nanoflakes are clearly discernible. Impressively, HRTEM unveils that the 2D carbon sheets are decorated with a large number of dark-contrast ultrafine Mo_2C particles (Figure 7d inset), similar to the original $Mo_2C/HNCFs$ (Figure 1e). There is no evidence that the long cycling results in the extensive aggregation.

3. Conclusion

In summary, we have developed a unique $Mo_2C/HNCFs$ composite configured with ultrafine Mo_2C nanoparticles uniformly dispersed on 2D nanosheets assembled 3D hollow N-doped carbon flowers and used it as multi-functional sulfur host for LSBs. Specifically, the ultrafine Mo_2C nanoparticles afford effective anchoring and catalytic active sites to LiPSs, which can not only enhance the LiPSs-adsorption ability but also accelerate the redox kinetics of polysulfide conversion during the cycling processes. Besides, the architecture of 2D nanosheets assembled 3D hollow N-doped carbon flowers contributes to Li^+ transportation and electrolyte infiltration. As a result, the $S-Mo_2C/HNCFs$ electrode retained a discharge capacity of 902 mAh g^{-1} after 100 cycles with 92% capacity retention. Moreover, the $Mo_2C/HNCFs$ composite exhibits a high rate capability of 1181 and 572 mA h g^{-1} at charge/discharge rates of 0.2C and 4C, respectively. Most impressively, the structural integrity of the hybrid flowers is largely preserved even after prolonged cycling. This work may open up a new avenue to design novel 3D host candidates with highly dispersed active sites on carbon network for advanced LSBs.

4. Experimental

12

Preparation of colloidal silica particles: Colloidal silica was prepared by using the classic Stöber method. In a typical preparation, 6mL of $NH_3 \cdot H_2O$ was added into a mixture of 24.75 mL of water and 16.75 m L of ethanol followed by adding the ethanolic solution of TEOS. Ethanolic solution of TEOS was prepared by dissolving 2.25 mL of TEOS in 45.5 mL of ethanol. The as-prepared colloidal silica was dispersed under ultrasound treatment in 60 mL of isopropanol and 200 μL of APTES. After ultrasound treatment, the reaction was kept for 2 h at 80 °C in an oil bath. The final product was obtained by centrifugation followed by washing, and freeze-drying.

Synthesis of Mo2C/HNCFs: Typically, 50 mg of the as-prepared amino-modified silica (SiO_2) particles were dispersed in 12 mL of ethanol under ultrasonication. Next ammonium molybdate tetrahydrate (185 mg) was dissolved in the mixed solvent of H_2O (18 mL) and ethanol (8 mL) and added into the ethanolic solution of SiO_2. Subsequently, 100 mg of dopamine dissolved in 18 mL of deionized water was added dropwise to the above solution. After 30 min, ammonia aqueous solution (0.5 mL) was added into the above mixture and continuously stirred at room temperature for 24 h. After the completion of the reaction, the product was collected by centrifugation, washed with DI water and ethanol, and dried at 70 °C overnight. The as-prepared solid product was carbonized at 350 °C with a heating rate of 3 °C min^{-1} for 3 h and then increased to 800 °C with a heating rate of 2 °C min^{-1} and kept for 2 h under an argon atmosphere. Next silica was removed from the carbonized product by treating with NaOH solution (4 M) for 4 h at 100 °C. The final product was washed with water and ethanol by vacuum filtration for several times and Mo2C/HNCFs was obtained after drying at 70 °C. The hollow nitrogen

13

doped carbon spheres (HNCS) as a control sample was prepared by following the same procedure except adding the ammonium molybdate tetrahydrate.

Formation of S-Mo₂C/HNCFs: Sulfur was loaded into Mo_2C/HNCFs composite by vapour phase infusion method. In brief sulfur powder and Mo_2C/HNCFs were mixed well by grinding and then sealed it in a glass vial. Finally heated the mixture at 300 ℃ for 4 hours under Ar and cool it at room temperature to get S-Mo_2C/HNCFs.

Structural characterizations: XRD patterns were recorded on a D8 FOCUS powder X-ray diffraction instrument (Burker AXS, Germany) using 40 Kv as tube voltage and 40 mA as tube current. FESEM equipped with EDS was performed on a Hitachi SU-70 microscope. The TEM was conducted on a JEOL JEM-2010 microscope at an accelerating voltage of 200 kV. XPS data were obtained on thermo scientific ESCALAB 250 XI electron spectrometer, using monochromatic Al Kα as exciting radiation at constant passing energy of 1486.6 Ev. TGA was conducted on NETZSCH, STA449 from room temperature to 800 °C with a heating rate of 10 $K\ min^{-1}$ in Ar.

Preparation of sulfur electrodes and electrochemical measurements: Sulfur electrode was prepared by mixing 70% S-Mo_2C/HNCFs, 20% super P and 10% poly (vinylidene fluoride) (PVDF, Sigma-Aldrich) binder in N-methyl 2-pyrrolidone (NMP, Sigma-Aldrich) solvent. Typical, S-Mo_2C/HNCFs and super P were mixed in a mortar by hand for long time followed by adding PVDF binder in NMP solvent to form a slurry. The slurry was then pasted on aluminum foil with the active material loading of ~1.5-1.8 mg cm^{-2} and then dried at 60 °C for 12 h. The electrode films were cut into round disks with a diameter of 8 mm. The standard 2025-type stainless steel coin cells were assembled inside an Ar-filled glovebox with lithium

14

metal foil as the negative electrode. The electrolyte was prepared by dissolving lithium bis-trifluoromethanesulphonylimide (LITFSI, 99%, Acros Organics, 1 M) and lithium nitrate (LiNO$_3$, 99.9%, Alfa Aesar, 0.1 M) in 1,2-dimethoxyethane (DME, 99.5%, Alfa Aesar) and 1,3-dioxolane (DOL, 99.5%, Alfa Aesar) (1:1 ratio, by volume). The amount of electrolyte is ~15 µL per mg sulfur. A LAND galvanostatic charge/discharge system was used. Stepwise rate performance was examined at different densities. The CV tests were performed on an SP-300 at different scan rates of (0.1 to 0.4 mV s^{-1}). EIS measurements were conducted on an SP-300 at a frequency range of 100 kHz to 100 mHz.

Symmetrical cell assembly and measurements: The electrodes were made by mixing the Mo$_2$C/HNCFs (without the presence of elemental sulfur) with PVDF in NMP at a weight ratio of 9:1 for symmetrical cells. The slurry was stirred well and pasted on aluminum foil with successive heating at 60 °C for 12 h. After drying, the electrode disks with a diameter of 12 mm were punched out and employed as working and reference electrodes. For the assembly of symmetrical cells, 40 µL of the electrolyte containing 0.5 mol L^{-1} Li$_2$S$_6$ and 1 mol L^{-1} LiTFSI in tetraglyme was used. The cyclic CV tests were performed on SP-300 at a scan rate of 50 mV s^{-1}. EIS measurements of symmetrical cells were performed at a frequency range of 100 kHz to 100 mHz on SP-300.

Supporting Information
Supporting Information is available from the Wiley Online Library or from the author.

References

1. Manthiram A, Fu Y, Chung SH, Zu C, Su YS. Rechargeable lithium-sulfur batteries. *Chem Rev*. 2014; 114:11751-11787.

2. Evers S, Nazar LF. New approaches for high energy density lithium-sulfur battery cathodes. *Acc Chem Res.* 2013; 46:1135-1143.

3. Sui R, Lavery CB, Li D, Deering CE, Chou N, Dowling NI, Marriott RA. Improving low-temperature CS_2 conversion for the Claus process by using La(III)-doped nanofibrous TiO_2 xerogel. *Appl Catal B.* 2019; 241:217-226.

4. Feng T, Zhao X, Wang T, Xia X, Zhang M, Huan Q. Reduction of SO_2 with CO to elemental sulfur in activated carbon bed. *Energy Fuels.* 2016; 30:6578-6584.

5. Gupta AK, Ibrahim S, Al Shoaibi. Advances in sulfur chemistry for treatment of acid gases. *Prog Energy Combust Sci.* 2016; 54:65-92.

6. Chung SH, Manthiram A. Current status and future prospects of metal-sulfur batteries. *Adv Mater.* 2019; 1:901125.

7. He J, Manthiram A. A review on the status and challenges of electrocatalysts in lithium-sulfur batteries. *Energy Storage Mater.* 2019; 20:55-70.

8. Sun Y, Liu N, Cui Y. Promises and challenges of nanomaterials for lithium-based rechargeable batteries. *Nature Energy*. 2016; 1:16071.

9. Lim WG, Kim S, Jo C, Lee J. A comprehensive review of materials with catalytic effects in Li-S batteries: Enhanced redox kinetics. *Angew Chem Int Ed.* 2019; 58:18746-18757.

10. Zhang H, Zou M, Zhao W, et al. Highly dispersed catalytic Co_3S_4 among a hierarchical carbon nanostructure for high-rate and long-life lithium-sulfur batteries. *ACS Nano.* 2019; 13:3982-3991.

11. Du Z, Chen X, Hu W, et al. Cobalt in nitrogen-doped graphene as single-atom catalyst for high-sulfur content lithium-sulfur batteries. *J Am Chem Soc.* 2019; 141:3977-3985.

12. Zhou G, Tian H, Jin Y, et al. Catalytic oxidation of Li_2S on the surface of metal sulfides for Li-S batteries. *Proc Natl Acad Sci U S A.* 2017; 114:840-845.

13. Al Salem H, Babu G, Rao CV, Arava LM. Electrocatalytic polysulfide traps for controlling redox shuttle process of Li-S batteries. *J Am Chem Soc.* 2015; 137:11542-11545.

14. Razaq R, Sun D, Xin Y, et al. Enhanced kinetics of polysulfide redox reactions on Mo_2C/CNT in lithium-sulfur batteries. *Nanotechnology.* 2018; 29:295401.

15. Razaq R, Sun D, Xin Y, et al. Ultrahigh sulfur loading in ZnS_{1-x}/rGO through in situ oxidation-refilling route for high-performance Li S batteries. *J Power Sources.* 2019; 414: 453-459.

16. Yang X, Gao X, Sun Q, et al. Promoting the transformation of Li_2S_2 to Li_2S: Significantly increasing utilization of active materials for high-sulfur- loading Li –S batteries. *Adv Mater.* 2019; 31:1901220.

17. Lim WG, Jo C, Cho A, et al. Approaching ultrastable high-rate Li-S batteries through hierarchically porous titanium nitride synthesized by multiscale phase separation. *Adv Mater.* 2019; 31:1806547.

18. Li BQ, Peng HJ, Chen X, et al. Polysulfide electrocatalysis on framework porphyrin in high-capacity and high-stable lithium-sulfur batteries.*CCS Chem.* 2019; 1:128-137.

17

19. Wang D, Zhao S, Li F, et al. Insight into the anchoring and catalytic effects of VO_2 and VS_2 nanosheets as sulfur cathode hosts for Li-S batteries. *Chem Sus Chem.* 2019; 12:4671-4678.

20. Yang H, Yang Y, Zhang X, et al. Nitrogen-doped porous carbon networks with active Fe-N_x sites to enhance catalytic conversion of polysulfides in lithium-sulfur batteries. *ACS Appl Mater Interfaces.* 2019; 11:31860-31868.

21. Ye Z, Jiang Y, Qian J, et al. Exceptional adsorption and catalysis effects of hollow polyhedra/carbon nanotube confined CoP nanoparticles superstructures for enhanced lithium-sulfur batteries. *Nano Energy*. 2019; 64:103965.

22. Liu H, Chen Z, Zhou L, et al. Interfacial charge field in hierarchical yolk-shell nanocapsule enables efficient immobilization and catalysis of polysulfides conversion. *Adv Energy Mater*. 2019; 9:1901667.

23. Zhou F, Li Z, Luo, T, et al. Low cost metal carbide nanocrystals as binding and electrocatalytic sites for high performance Li-S batteries. *Nano Lett.* 2018;v18:1035-1043.

24. Cao B, Chen Y, Li D, Yin L, Mo Y. Synthesis of TiC nanoparticles anchored on hollow carbon nanospheres for enhanced polysulfide adsorption in Li-S batteries. *Chem Sus Chem* 2016; 9:3338-3344.

25. Balach J, Linnemann J, Jaumann T, Giebeler L. Metal-based nanostructured materials for advanced lithium–sulfur batteries. *J Mater Chem* A. 2018; 6: 23127-23168.

26. Wu Y, Zhu X, Li P, et al. Ultradispersed W_xC nanoparticles enable fast polysulfide interconversion for high-performance Li-S batteries. *Nano Energy.* 2019; 59:636-643.

27. Huang Y, Gong Q, Song X, et al. Mo₂C nanoparticles dispersed on hierarchical carbon microflowers for efficient electrocatalytic hydrogen evolution. *ACS Nano*. 2016; 10:11337-11343.

28. Li JS, Wang Y, Liu CH, et al. Coupled molybdenum carbide and reduced graphene oxide electrocatalysts for efficient hydrogen evolution. *Nat Commun*. 2016; 7:11204.

29. Yang X, Li Q, Lu E, et al. Taming the stability of Pd active phases through a compartmentalizing strategy toward nanostructured catalyst supports. *Nat Commun.* 2019; 10:1611.

30. Wu X, Si Y, Zou Y, et al. Dual-porosity hollow carbon spheres with tunable through-holes for multi-guest delivery. *ACS Appl Mater Interfaces* 2018; 10:31664-31673.

31. Xin H, Hai Y, Li D, et al. Coupling Mo₂C@C core-shell nanocrystals on 3D graphene hybrid aerogel for high-performance lithium ion battery. *Appl Surf Sci.* 2018; 441:69-76.

32. Amiinu IS, Pu Z, Liu X, et al. Multifunctional Mo-N/C@MoS₂ electrocatalysts for HER, OER, ORR, and Zn-air batteries. *Adv Funct Mater.* 2017; 27:1702300.

33. Qing Gao X.Z, Xiao Y, Zhao D, Cao M, A mild route to mesoporous Mo₂C-C hybrid nanospheres for high performance lithium-ion batteries. *Nanoscale.* 2014; 6:6151-6157.

34. Cui Z, Zu C, Zhou W, Manthiram A, Goodenough JB. Mesoporous titanium nitride-enabled highly stable lithium-sulfur batteries. *Adv Mater.* 2016; 28:6926-6931.

35. Peng H-J, Huang J-Q, Cheng X-B, Zhang Q, Review on high-loading and high-energy lithium-sulfur batteries, *Adv. Energy Mater*. 2017; 7:1700260.

36. Yin L-C, Liang J, Zhou G-M, Li F, Saito R, Cheng H-M, Understanding the interactions between lithium polysulfides and N-doped graphene using density functional theory calculations, *Nano Energy*. 2016; 25:203-210.

37. Hou T-Z, Xu W-T, Chen X, Peng H-J, Huang J-Q, Zhang Q, Lithium bond chemistry in lithium-sulfur batteries, *Angew Chem Int Ed*. 2017; 56:8178-8182.

38. Fan FY, Carter WC, Chiang YM. Mechanism and kinetics of Li_2S precipitation in lithium-sulfur batteries. *Adv Mater*. 2015; 27:5203-5209.

39. Yuan Z, Peng HJ, Hou TZ, et al. Powering lithium-sulfur battery performance by propelling polysulfide redox at sulfiphilic hosts. *Nano Lett*. 2016; 16:519-527.

40. Huang X, Tang J, Luo B, et al. Sandwich-like ultrathin TiS_2 nanosheets confined within N, S codoped porous carbon as an effective polysulfide promoter in lithium-sulfur batteries. *Adv Energy Mater*. 2019; 9:1901872.

41. Zhang Z-W, Peng H-J, Zhao M, Huang J-Q, Heterogeneous/homogeneous mediators for high-energy-density lithium-sulfur batteries: Progress and prospects, *Adv. Funct. Mater*. 2018; 28:1707536.

42. Li S-Y, Wang W-P, Duan H, Guo Y-G, Recent progress on confinement of polysulfides through physical and chemical methods, *J. Energy Chem*. 2018; 27:1555-1565.

43. Li Y, Xu P, Chen G, et al. Enhancing Li-S redox kinetics by fabrication of a three dimensional Co/CoP@nitrogen-doped carbon electrocatalyst. *Chem Eng J*. 2020; 380:122595.

44. Zeng Z, Li W, Wang Q, Liu X. Programmed Design of a Lithium–Sulfur Battery Cathode by Integrating Functional Units. *Adv Sci*.2019; 6:1900711.

45. Song Y, Zhao W, Zhu X, et al. Vanadium dioxide-graphene composite with ultrafast anchoring behavior of polysulfides for lithium-sulfur batteries. *ACS Appl Mater Interfaces.* 2018; 10:15733-15741.
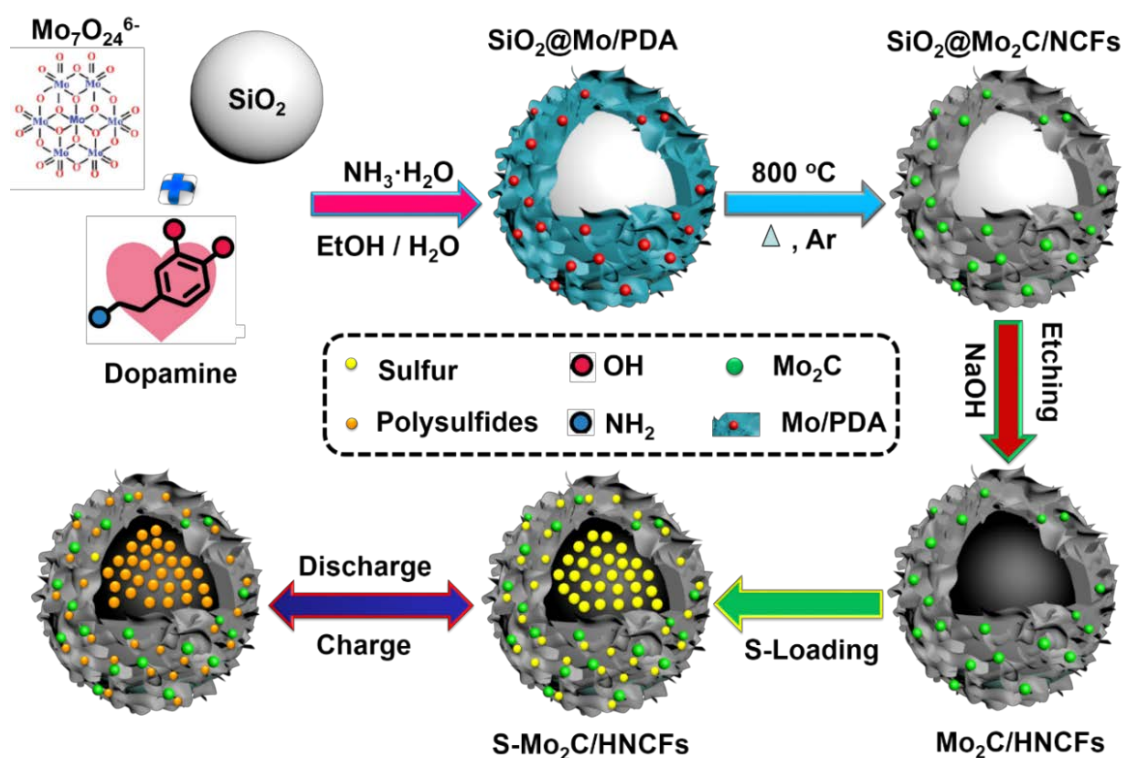
Scheme 1. Schematic illustration for the preparation of Mo$_2$C/HNCFs, sulfur loading using vapour phase infusion method and electrochemical redox process.
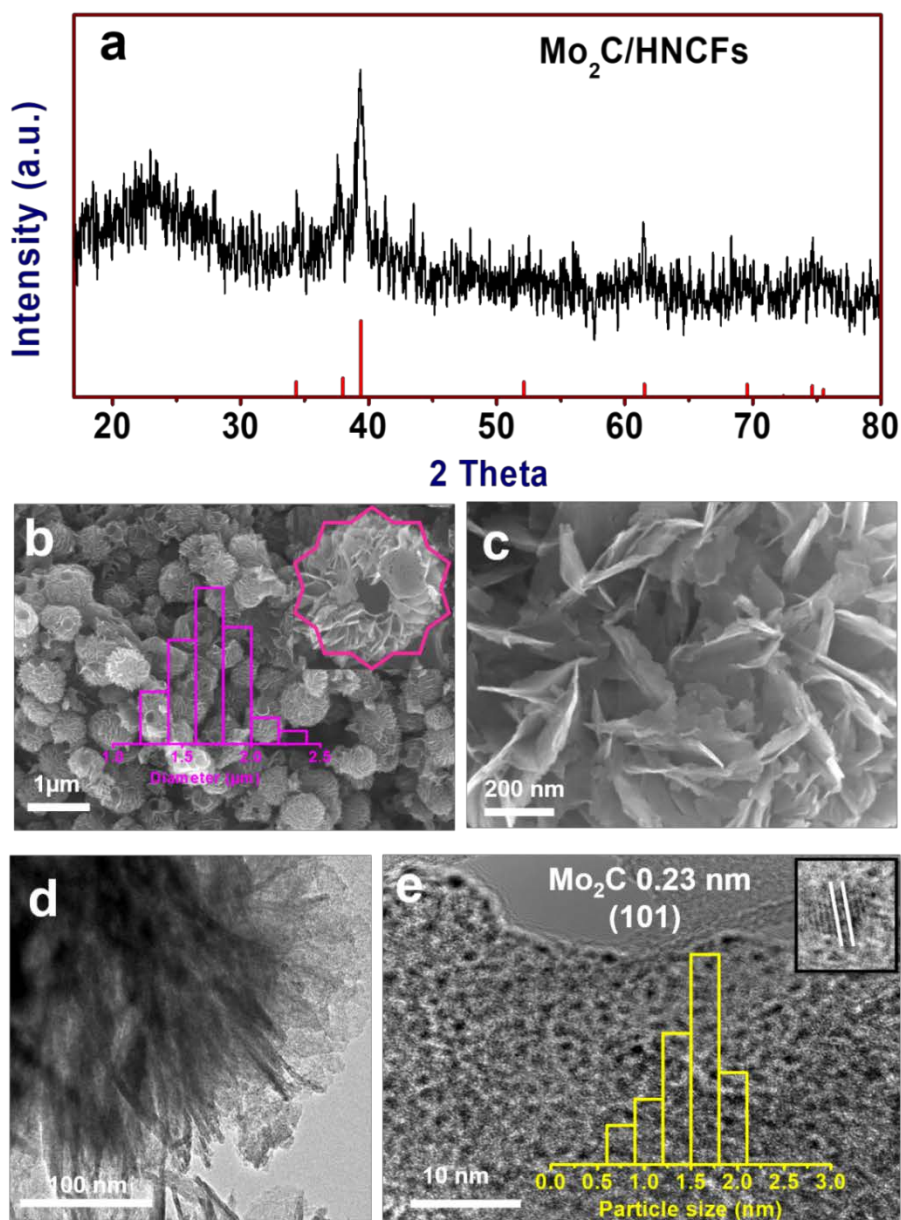
Figure 1. XRD pattern (a), FESEM images (b, c) and TEM images (d, e) of Mo$_2$C/HNCFs.
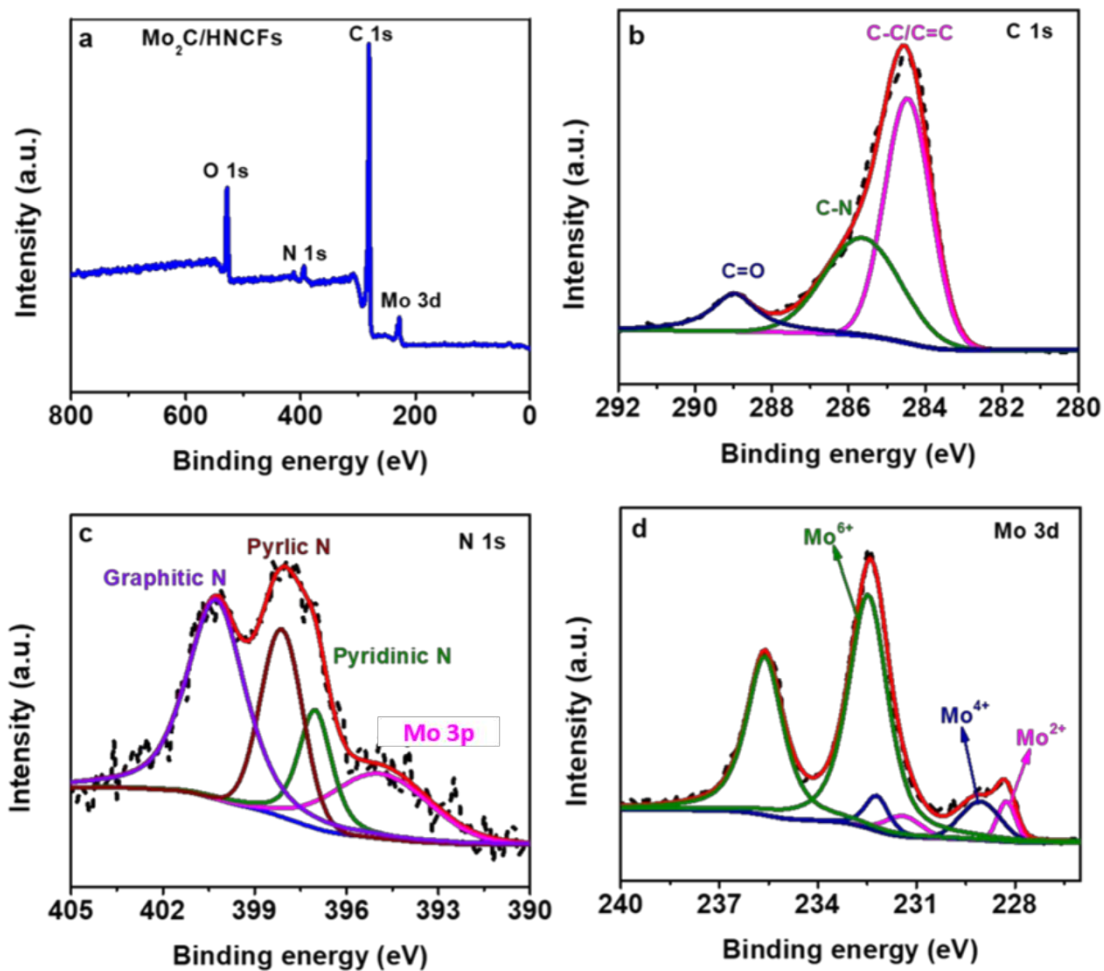
Figure 2. XPS survey spectra (a), high-resolution XPS spectra of C 1s (b), N 1s (c), and Mo 3d (d) of Mo_2C/HNCFs.
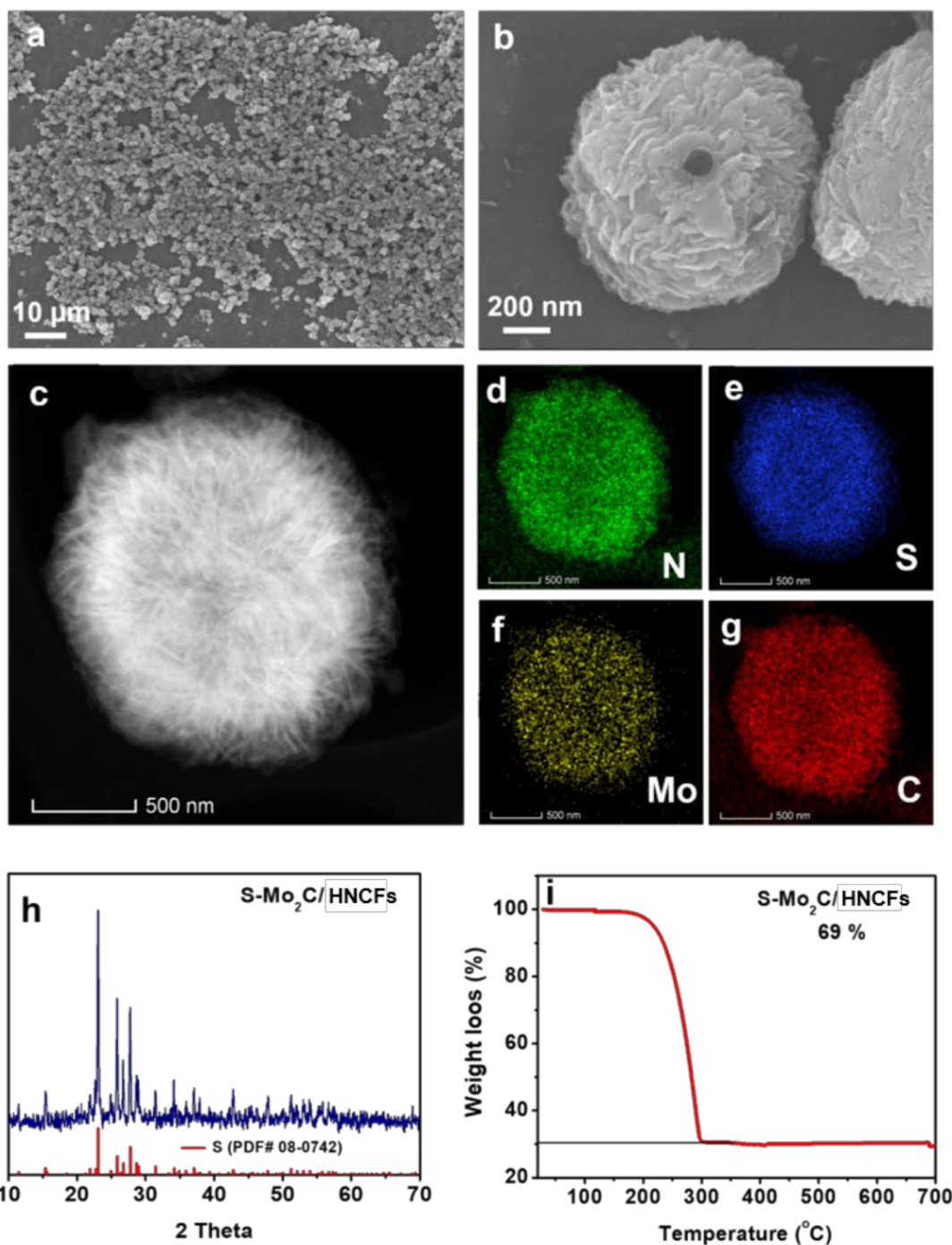
Figure 3. FESEM images (a, b), STEM image and the corresponding element mapping (c-g),

XRD pattern (h) and TGA curve (i) of S-Mo$_2$C/HNCFs.

26
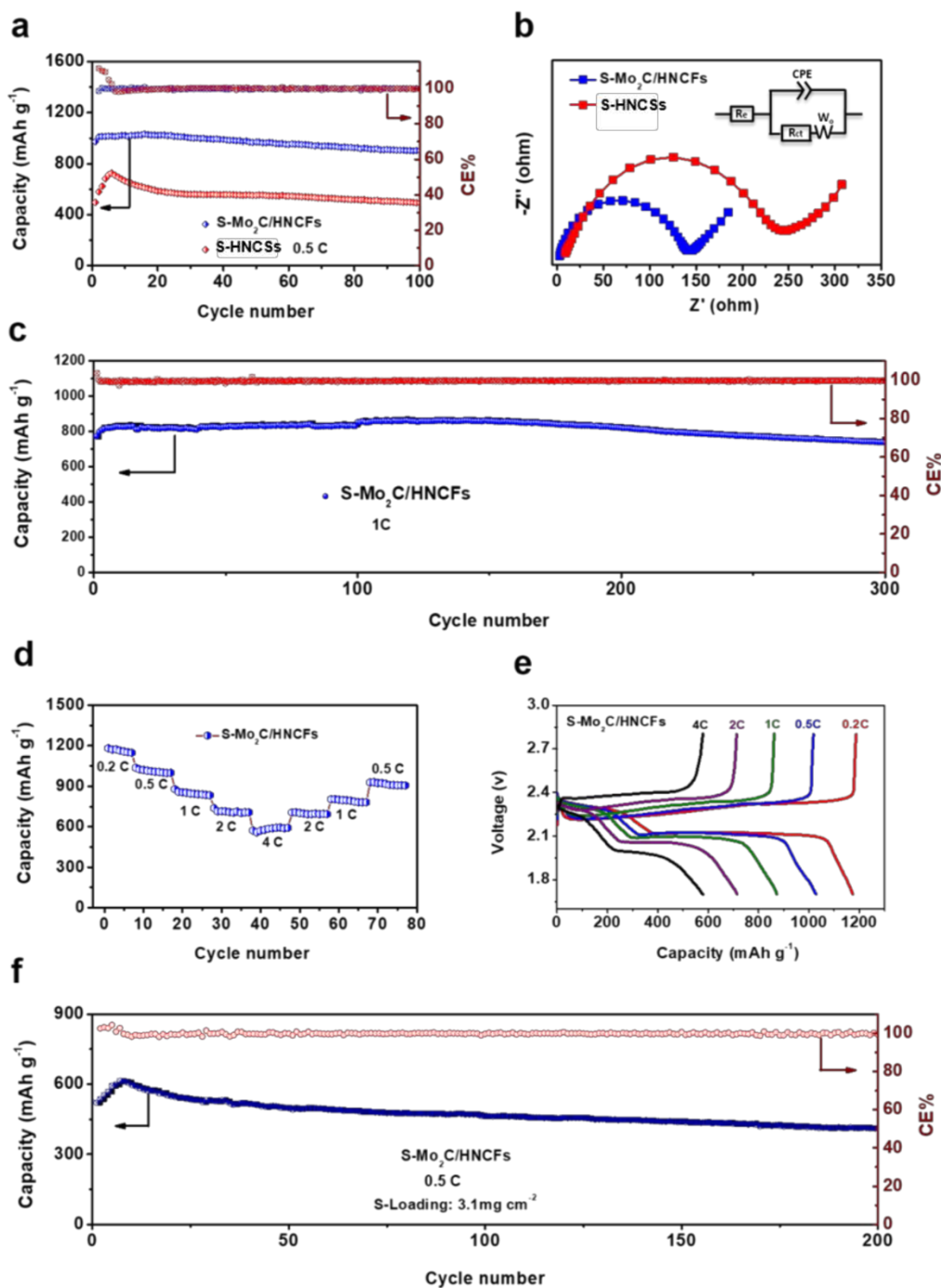
Figure 4. Cycling performance and Coulombic efficiency (CE) at 0.5 C for 100 cycles (a),

Electrochemical impedance spectroscopy (EIS) (b) for the S-Mo$_2$C/HNCFs and S-HNCSs

cathodes, long cycling performance and CE of the S-Mo$_2$C/HNCFs cathode at 1C for 300

cycles (c), rate performance (d) and Galvanostatic discharge-charge curves (e) of the S-

Mo$_2$C/HNCFs cathode at different current densities, cycling performance and CE of S-

Mo$_2$C/HNCFs at 3.1 mg cm^{-2} areal sulfur loading for 200 cycles (f).

28
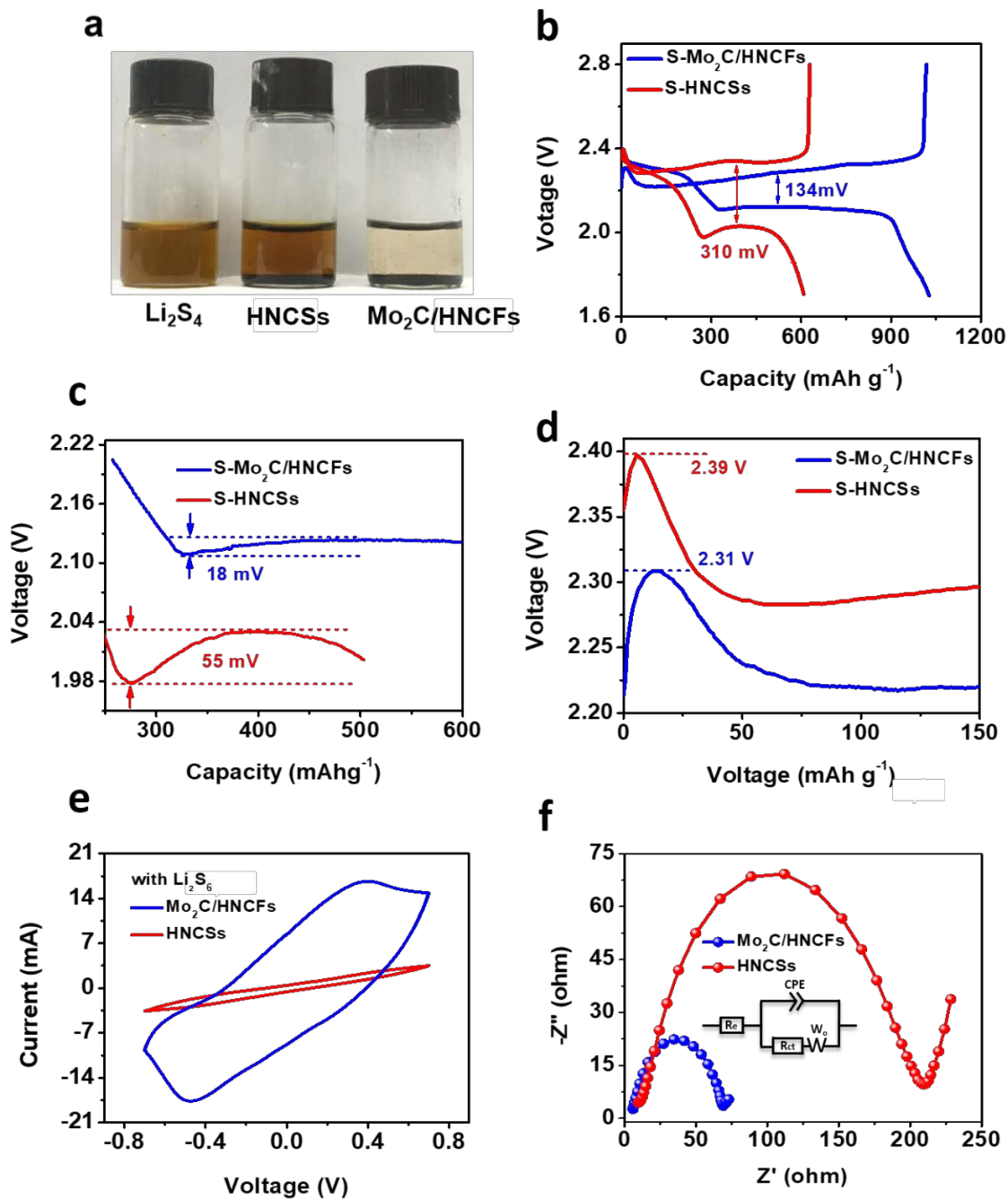
Figure 5. Catalytic effects of Mo$_2$C/HNCFs on LPSs conversion. Visualized adsorption of Li$_2$S$_4$ on HNCSs and Mo$_2$C/HNCFs (a), discharge and charge profiles of S-Mo$_2$C/HNCFs and S-HNCSs electrodes (c-d), polarization curves (e) and EIS (f) of symmetrical cells for HNCSs and Mo$_2$C/HNCFs.
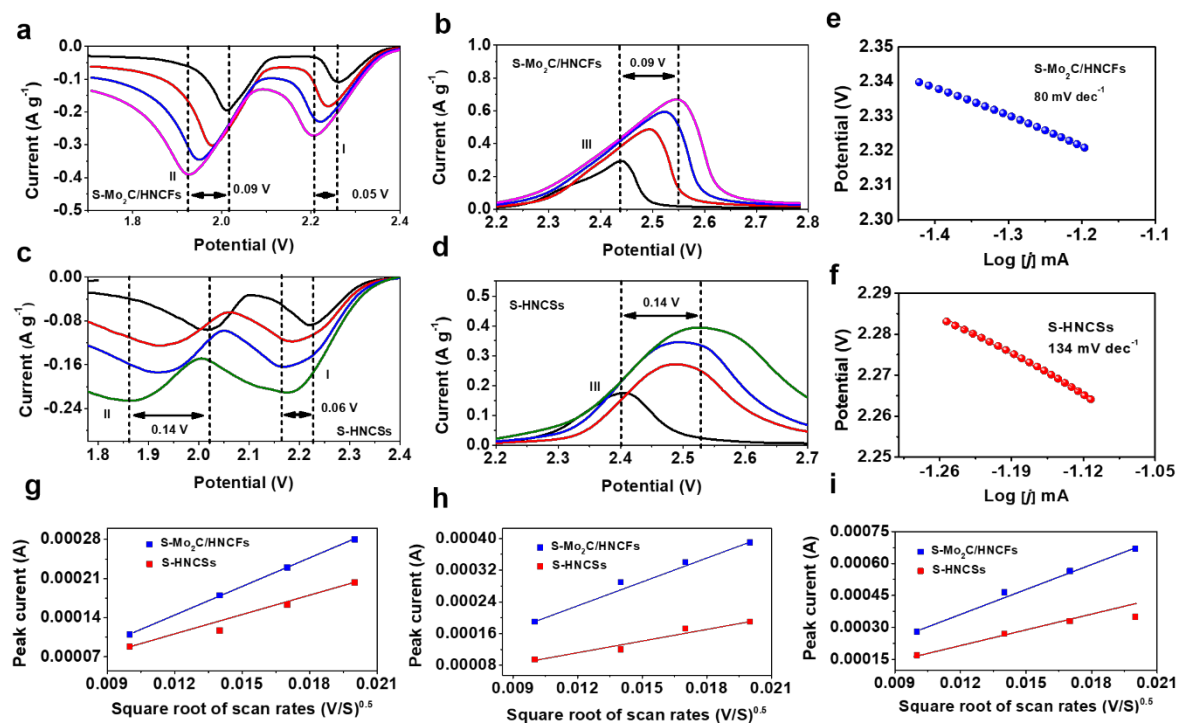
Figure 6. Catalytic effects of Mo$_2$C/HNCFs on redox kinetics of LPSs conversion. The CV data of S-Mo$_2$C/HNCFs (a, b) and S-HNCSs (c, d) electrodes at different scan rates. Tafel plots of S-Mo$_2$C/HNCFs (e) and S-HNCSs (f). Reaction kinetics with respect to the Li$^+$ ion diffusion properties at various voltage scan rates. The cathodic reaction I (S$_8$-Li$_2$S$_4$) (g), the cathodic reaction II (Li$_2$S$_4$-Li$_2$S) (h), and the anodic reaction III (Li$_2$S-S$_8$) (i).

30
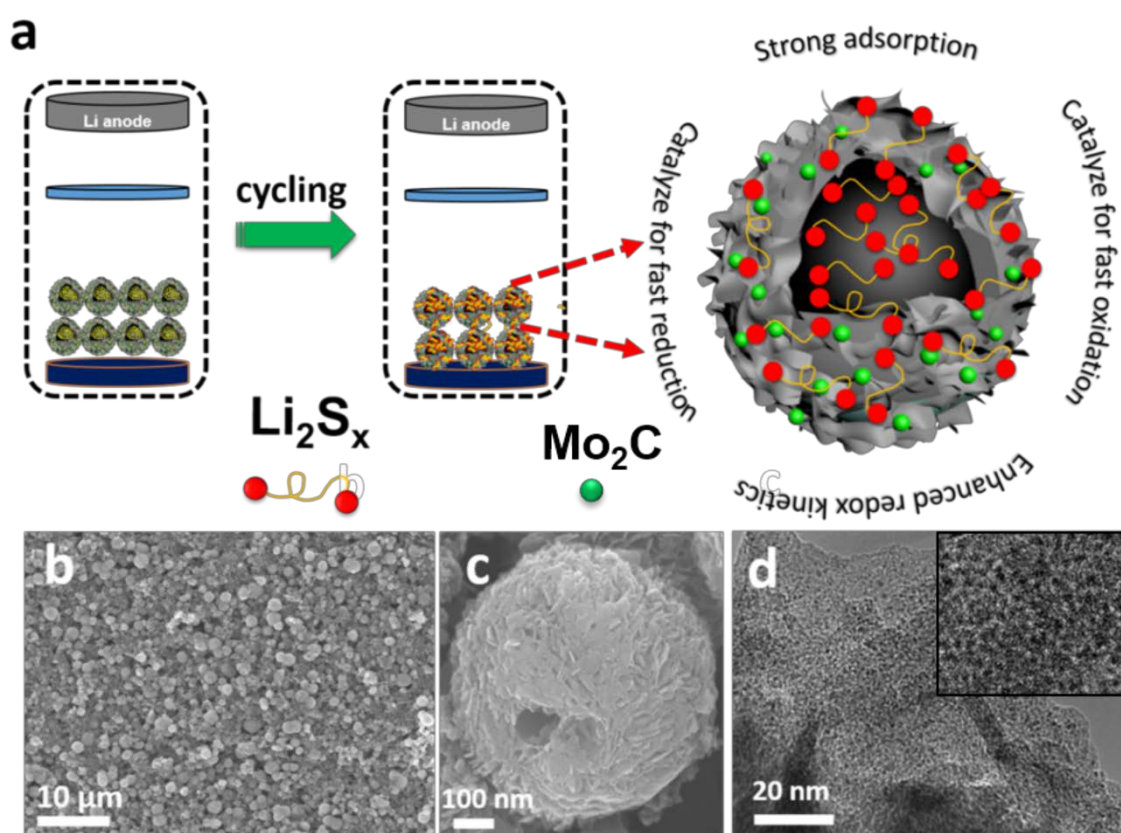
Figure 7. Schematic illustration of the mechanisms during redox reaction (a), FESEM images of Mo$_2$C/HNCFs (b, c), and HRTEM image (d) after cycling.

31

Ultrafine Mo_2C nanoparticles on hollow N-doped carbon flowers has been employed as an efficient catalytic active sites for conversion of LPSs, which can not only enhance the LPSs-adsorption ability but also accelerate the redox kinetics of polysulfide conversion. Besides, the unique architecture of 2D nanosheets assembled 3D hollow N-doped carbon flowers contributes to Li^+ transportation and electrolyte infiltration.

Keywords

lithium-sulfur battery, electrocatalysis, ultrafine Mo_2C, 3D nanostructure, polysulfide conversion

Electrocatalytic conversion of lithium polysulfides by highly dispersed ultrafine Mo_2C nanoparticles on hollow N-doped carbon flowers for Li-S batteries
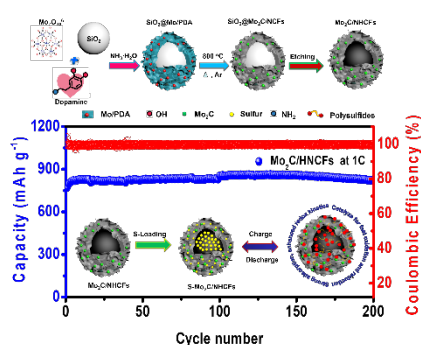
ToC figure (Please choose one size: 55 mm broad × 50 mm high **or** 110 mm broad × 20 mm high. Please do not use any other dimensions)
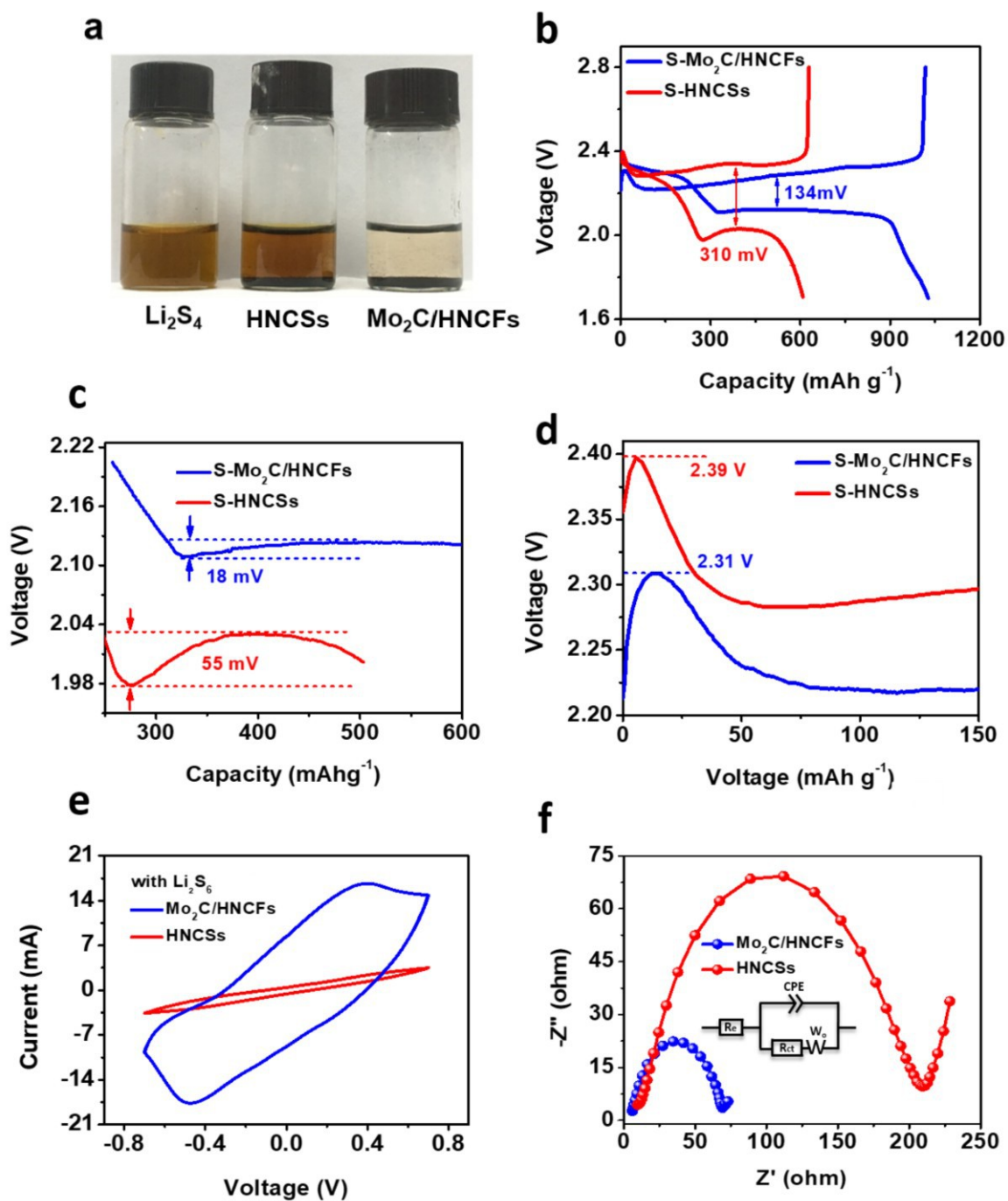
32
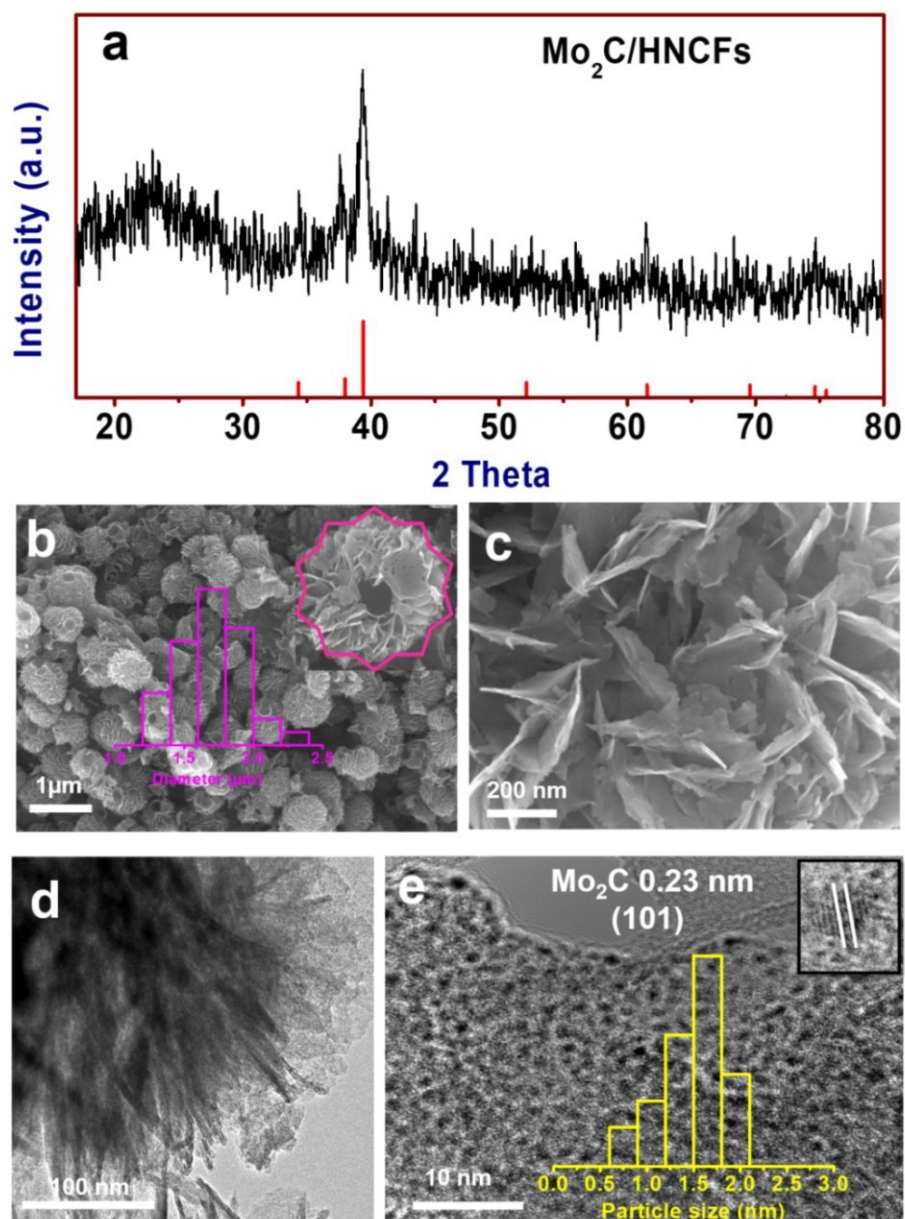
EOM2_12020_figure 1.jpg
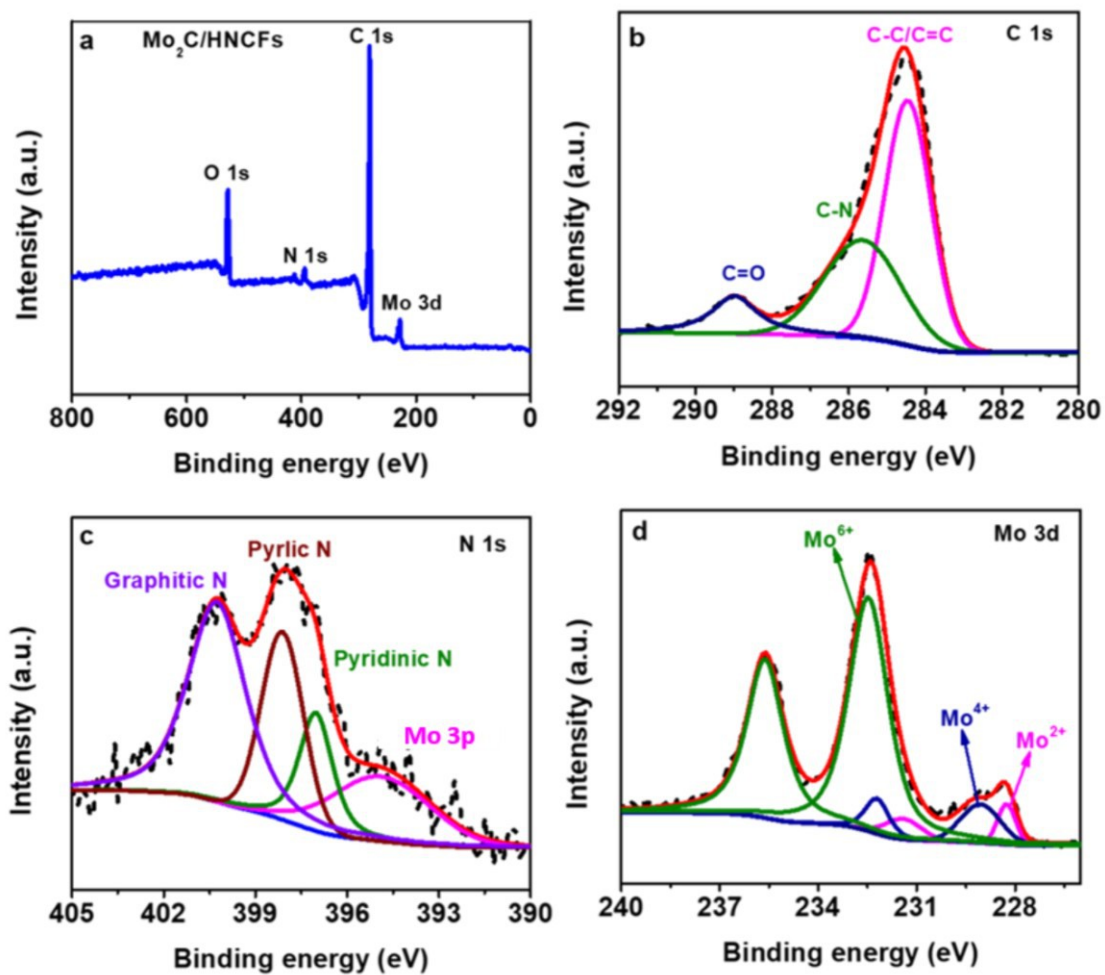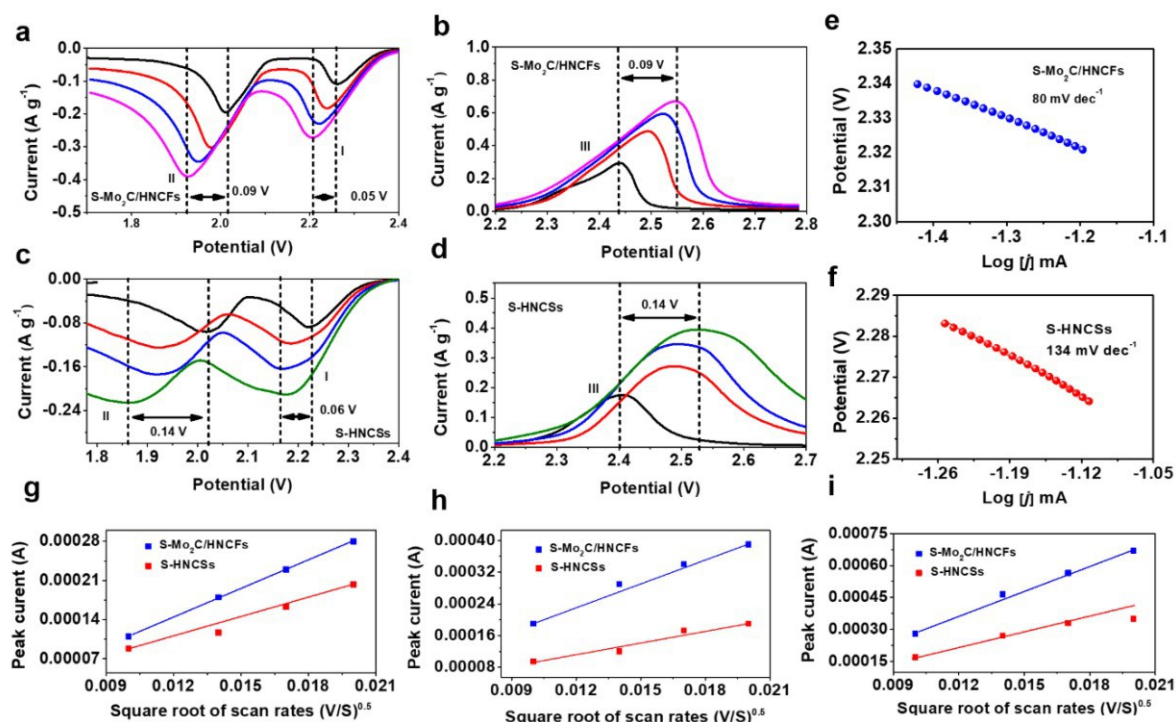
EOM2_12020_figure 2.jpg
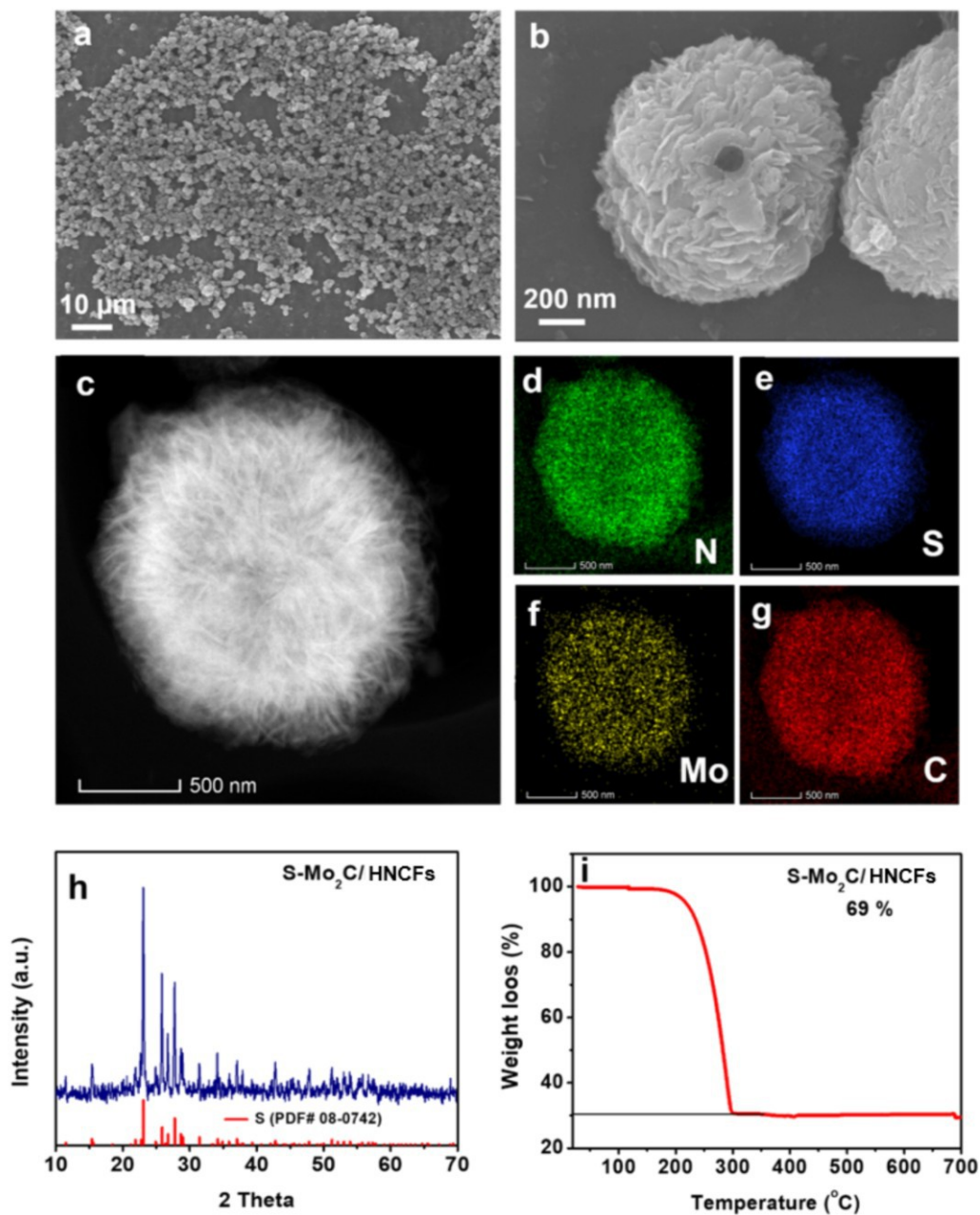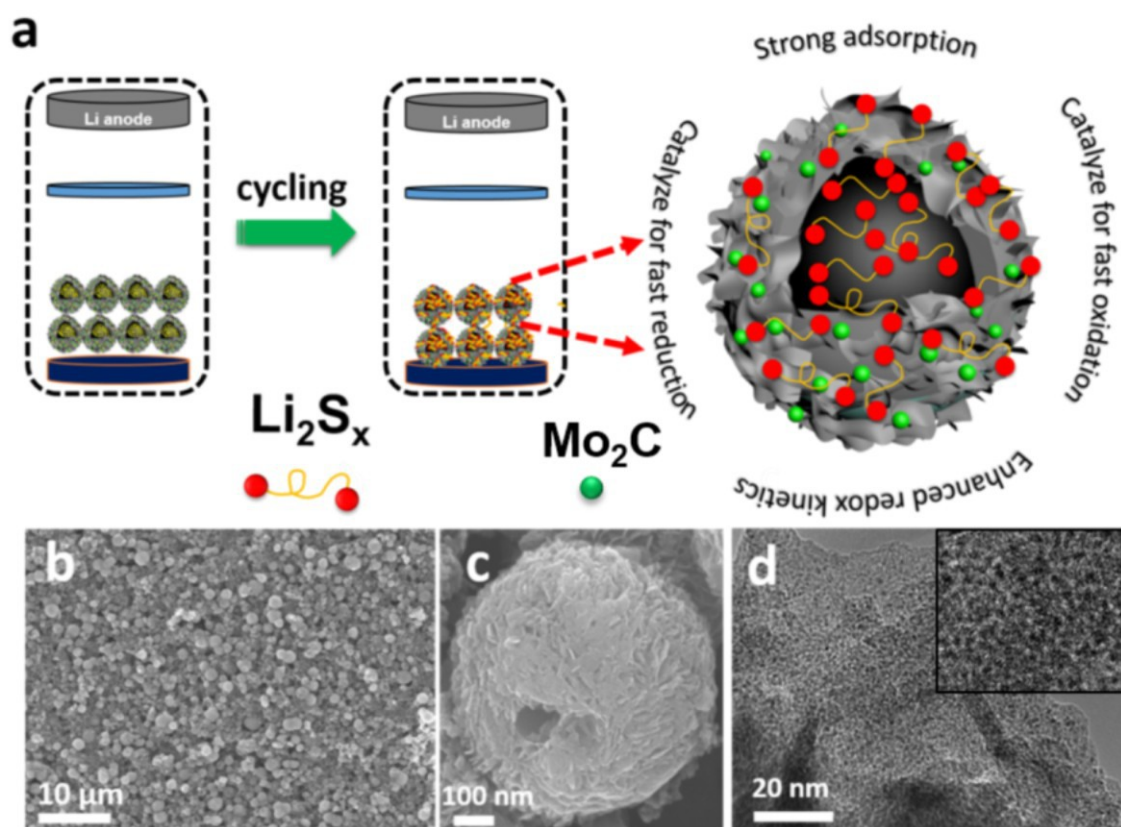
EOM2_12020_figure 3.jpg
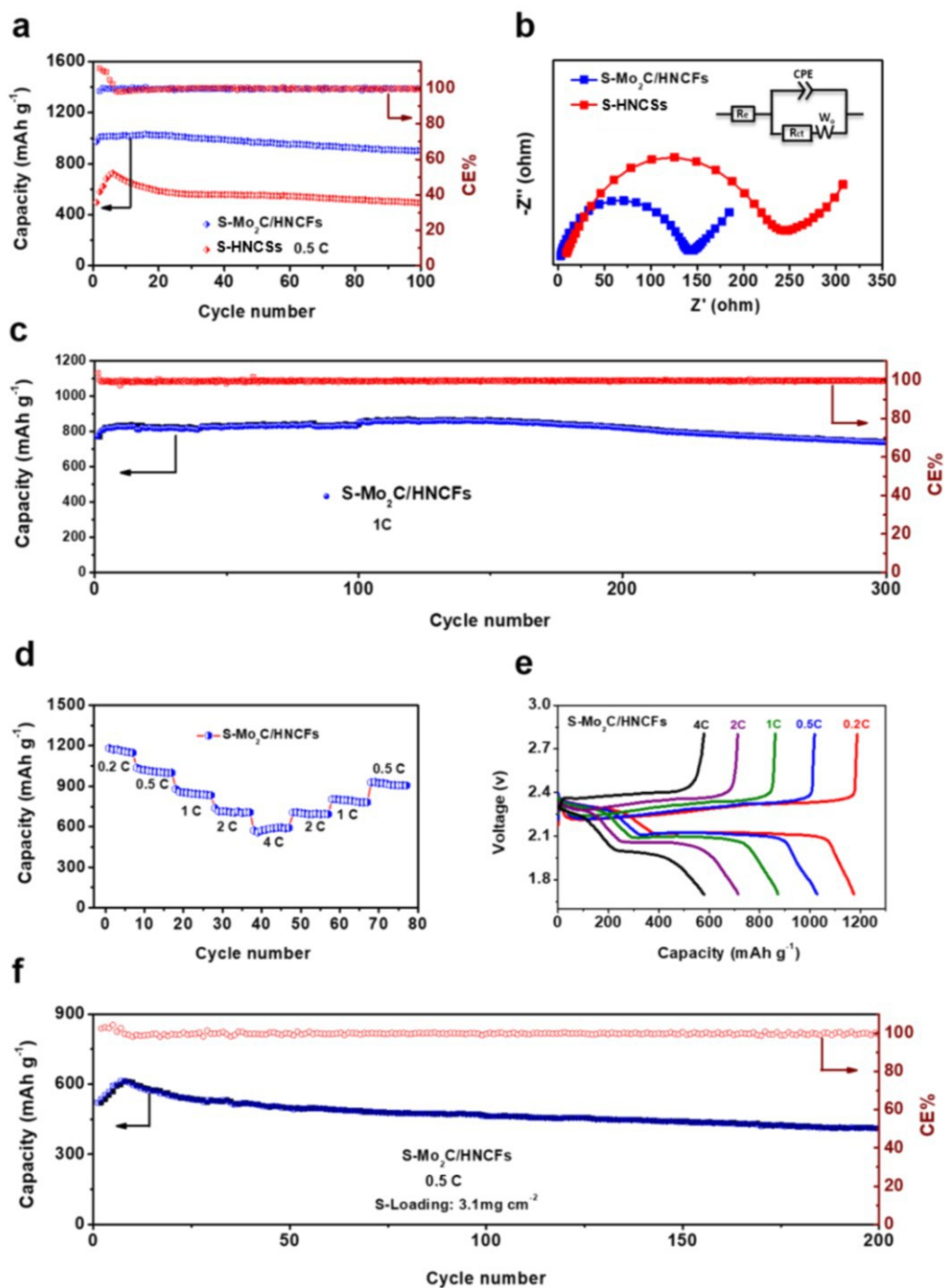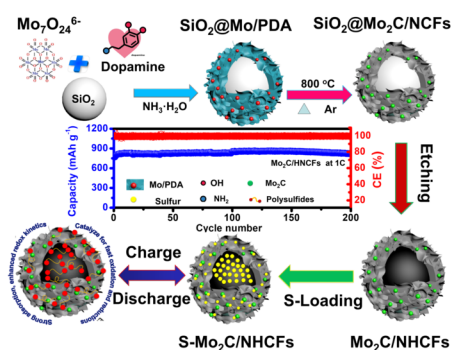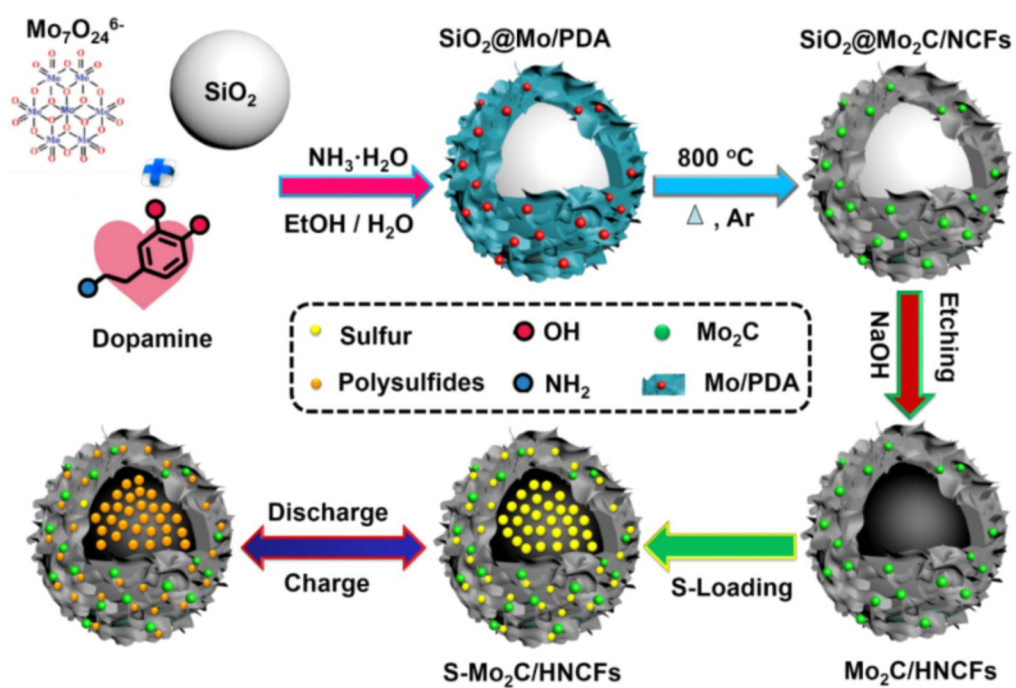
EOM2_12020_figure 4.jpg

EOM2_12020_figure 5.jpg

EOM2_12020_figure 6.jpg

EOM2_12020_figures 7.jpg

EOM2_12020_For Table of Contents Only.tif

EOM2_12020_scheme 1.jpg